

1 **Principal Component Analysis to Determine the Surface Properties that Influence the**  
2 **Self-Cleaning Action of Hydrophobic Plant Leaves**

3  
4  
5  
6 Fabien Saubade<sup>a</sup>, Lisa I. Pilkington<sup>b</sup>, Christopher M. Liauw<sup>a</sup>, Luciana Gomes<sup>c</sup>, Jake  
7 McClements<sup>d</sup>, Marloes Peeters<sup>d</sup>, Mohamed El Mohtadi<sup>e</sup> Filipe Mergulhão<sup>c</sup> and Kathryn A.  
8 Whitehead<sup>a\*</sup>

9  
10  
11 <sup>a</sup> Microbiology at Interfaces, Department of Life Sciences, Manchester Metropolitan  
12 University, Manchester, UK.

13 <sup>b</sup> School of Chemical Sciences, University of Auckland, Auckland 1010, New Zealand

14 <sup>c</sup> LEPABE, Department of Chemical Engineering, Faculty of Engineering, University of  
15 Porto, Portugal

16 <sup>d</sup> School of Engineering, Newcastle University, Merz Court, Claremont Road, Newcastle  
17 Upon Tyne NE1 7RU, UK

18 <sup>e</sup> Department of Biology, Edge Hill University, Ormskirk, Lancashire, L39 4QP, UK

19  
20 \*Corresponding Author: K. A. Whitehead, Manchester Metropolitan University, UK.

21 E-mail address [K.A.Whitehead@mmu.ac.uk](mailto:K.A.Whitehead@mmu.ac.uk)

23 **ABSTRACT**

24 It is well established that many leaf surfaces display self-cleaning properties. However, an  
25 understanding of how the surface properties interact is still confounding. Consequently, twelve  
26 different leaf types were selected for analysis due to their water repellency and self-cleaning  
27 properties. The most hydrophobic surfaces demonstrated splitting of the  $\nu_s$  CH<sub>2</sub> and  $\nu$  CH<sub>2</sub>  
28 bands, ordered platelet-like structures, crystalline waxes, high surface roughness values, high  
29 total surface free energy and apolar components of surface energy, and low polar and Lewis  
30 base components of surface energy. The surfaces that exhibited the least roughness and high  
31 polar and Lewis base components of surface energy had intracuticular waxes, yet still  
32 demonstrated self-cleaning action. Principal component analysis demonstrated that the most  
33 hydrophobic species shared common surface chemistry traits with low intra-class variability,  
34 whilst the less hydrophobic leaves had highly-variable surface chemistry characteristics.  
35 Despite this, we have shown through partial least squares regression that leaf water contact  
36 angle (i.e. hydrophobicity) can be predicted using attenuated total reflectance Fourier transform  
37 infrared spectroscopy surface chemistry data with excellent ability. This is the first time that  
38 such a statistical analysis has been performed on a complex biological system. This model  
39 could be utilised to investigate and predict the water contact angles of a range of biological  
40 surfaces. An understanding of the interplay of properties is extremely important when  
41 producing optimised biomimetic surfaces.

42

43 **Keywords:** Biomimetic; plant; roughness; superhydrophobic; wax; self-cleaning.

44

## 45 INTRODUCTION

46       There has been significant interest directed towards producing biomimetic surfaces  
47 with controlled surface wetting properties.<sup>1</sup> Much of this work has concentrated on altering  
48 surface topography and chemistry to produce superhydrophobic surfaces. It is generally  
49 considered that the topography of plant surfaces is the main factor influencing water contact  
50 angle, and hence water repellency.<sup>2,3</sup> Specifically, hierarchical structures at the macro and  
51 micro levels (the Lotus effect) are associated with superhydrophobicity of leaf surfaces.<sup>4</sup> The  
52 leaves are also self-cleaning, meaning that rolling droplets can remove microorganisms and  
53 other contaminants from their surfaces. Numerous biomimetic surfaces have been developed  
54 which emulate the topography of superhydrophobic leaves to achieve self-cleaning, water  
55 repellency, and anticontamination properties.<sup>5-8</sup> However, many self-cleaning surfaces  
56 produced with biomimetic topographies still require chemical modification to exhibit  
57 superhydrophobicity. Many plant surfaces are hydrophobic (WCA  $>110^\circ$ ) or  
58 superhydrophobic (WCA  $>150^\circ$ ).<sup>9</sup> However, in nature, there are also several leaf surfaces that  
59 display self-cleaning and water-repellent behaviours, and yet they are not superhydrophobic  
60 and may not have predominant topographical features.

61       It is well established that the wax layer on leaf surfaces, in particular epicuticular wax  
62 crystals, makes an essential contribution to surface hydrophobicity.<sup>10</sup> The chemical  
63 compositions of such waxes from numerous leaf surfaces have been determined.<sup>11-17</sup> However,  
64 the exact relationship between the surface chemistry and topography, in addition to their  
65 influence on surface physiochemistry is not fully understood. Consequently, producing  
66 biomimetic surfaces that maintain their anti-wetting features still presents a significant  
67 challenge. Thus, an understanding of the key surface properties that result in the water  
68 repellency of natural surfaces is essential to further the development of biomimetic surfaces.

69           The aim of this work was to determine the relationship between the surface topography,  
70 chemistry, and physiochemistry of a selection of plant leaves that demonstrated self-cleaning  
71 properties. This was implemented through a combination of complimentary experimental  
72 techniques and modelling methods to identify the key parameters that resulted in the self-  
73 cleaning properties of these natural surfaces. This information is vitally important to many  
74 aspects of industry where producing low-cost and consistent biomimetic surfaces is a priority.

75

## 76 **EXPERIMENTAL**

### 77 *Leaf collection*

78           Plant leaves were selected based on their ability to repel water. Many leaf types were  
79 sprayed with water for 1 min and then immediately assessed. Those that exhibited no residual  
80 water droplets or spherical spray droplets on their surfaces were deemed the most hydrophobic,  
81 and therefore selected. Leaves from the following plants were collected (Westhoughton,  
82 Greater Manchester, UK) between the months of September and November 2017: *Aquilegia*  
83 *vulgaris* (Aquilegia), *Citrus sinensis* (Orange), *Gladiolus hybridus* (Gladioli), *Hosta*  
84 *sieboldiana* (Hosta), *Hyacinthus litwinovii* (Hyacinth), *Ilex aquifolium* (Holly), *Lathyrus*  
85 *odoratus* (Sweet pea), *Lupinus polyphyllus* (Lupin), *Nymphaea odorata* (Water lily),  
86 *Pelargonium graveolens* (Geranium), *Prunus laurocerasus* (Laurel), and *Rhododendron*  
87 *azaleastrum* (Azalea). Leaf samples were either used within 2-4 h of harvesting or stored at 4  
88 °C for a maximum of 24 h before use. The leaves were stored individually in plastic bags until  
89 use to ensure that the loss of humidity from the leaf was reduced. A number of separate batches  
90 of mature leaves were collected on different days over the two-month experimental period ( $n$   
91 = 10).

92

### 93 *Determination of surface energy components*

94 The total surface free energy ( $\gamma_s$ ) and the apolar ( $\gamma_s^{LW}$ ), polar ( $\gamma_s^{AB}$ ), Lewis acid ( $\gamma_s^+$ ),  
95 and Lewis base ( $\gamma_s^-$ ) free energy components of the adaxial surfaces of the leaves were  
96 determined using contact angle goniometry. The surface energy components of the leaves were  
97 calculated according to work by van Oss and colleagues.<sup>18-20</sup> A KRÜSS sessile drop  
98 goniometer (GH11 KRÜSS, France) was used to perform the measurements with three test  
99 liquids: HPLC grade water (BDH, UK), formamide (Sigma-Aldrich, UK), and diiodomethane  
100 (Alfa Aesar, UK). For each plant species, except the *Rhododendron azaleastrum*, samples were  
101 cut from different parts of the same leaf and attached to microscope slides using double-sided  
102 adhesive tape (3M, UK). In the case of *Rhododendron azaleastrum*, individual leaves were  
103 used for each test liquid. For all test liquids, the droplet volume was 5  $\mu$ L and was dispensed  
104 using a micro-syringe dedicated to a single solvent.

105 For each plant species, the van Oss and Good equations were used to obtain the surface  
106 energy components from the contact angles of the three test liquids on the leaf surfaces.<sup>18-20</sup>  
107 The surface free energy components of these three liquids were taken from Bos et al.<sup>21</sup>  
108 (Supporting Information: Table S1).

109 The contact angles of each test liquid were obtained from five different areas on the  
110 leaf, therefore average values were used to obtain the physicochemical parameters. The  
111 statistical error in the calculated surface energy components was estimated from the contact  
112 angles of each test liquid by using propagation of error principles. The interfacial free energy  
113 ( $\Delta G_{iwi}$ ) was used as a measure of the hydrophobicity of a leaf surface where greater (negative)  
114  $\Delta G_{iwi}$  values related to more hydrophobic surfaces.

115

### 116 *Optical profilometry and scanning electron microscopy (SEM)*

117 The surface topographies of the leaves were investigated using a previously described  
118 method with a MicroXAM (phase shift) surface mapping microscope (ADE corporation, XYZ

119 model 4400 ml system, USA).<sup>22</sup> The optical profilometer used an AD phase shift controller  
120 (Omniscan, UK). A MAPVIEW AE 2.17 (Omniscan, UK) image analysis system was utilised  
121 to obtain the average surface roughness ( $S_a$ ), root mean square roughness ( $S_q$ ), and average  
122 peak-to-valley roughness ( $S_{pv}$ ) (n=10).

123 SEM images were obtained using a Supra 40VP SEM (Carl Zeiss Ltd., UK) with an  
124 adapted protocol.<sup>23</sup> The leaf samples were soaked for 24 h at 4 °C in 4 % v/v glutaraldehyde  
125 (Agar Scientific, UK). The leaf samples were removed and the excess glutaraldehyde was  
126 washed from the leaf surface using sterile water. The leaf samples were then dried overnight.  
127 Following drying, the samples were cut into ca. 6 mm<sup>2</sup> coupons. The adaxial sides of the leaves  
128 were fixed to carbon pads on SEM stubs (Agar Scientific, UK). The fixed leaf surfaces were  
129 sputter coated with gold (Polaron, UK) using the parameters: 5 mA, < 0.1 mbar, and 800 V in  
130 argon gas.

131

### 132 *Attenuated total reflectance Fourier transform infrared spectroscopy (ATR-FTIR)*

133 ATR-FTIR analysis was performed on leaf samples using a Spectrum Two FT-IR  
134 Spectrometer (PerkinElmer, UK) fitted with a UATR single bounce ATR accessory with a  
135 diamond (refractive index 2.40) internal reflection element (IRE) (45° angle of incidence) and  
136 LiTaO<sub>3</sub> detector. For each leaf sample, five different areas were analysed obtaining the spectra  
137 over the range of 450 to 4000 cm<sup>-1</sup>. Spectra were made up of four scans with the resolution set  
138 to 4 cm<sup>-1</sup> and the results were expressed in absorbance. It is worth noting that the penetration  
139 depth of the evanescent wave into the leaf surface from the IRE can be estimated to be 1.5 µm  
140 at 2900 cm<sup>-1</sup> and 6.1 µm at 700 cm<sup>-1</sup>. Calculations based on the equation by F.Mirabella  
141 assumed the leaf surface to be mainly hydrocarbon, i.e. paraffin wax (refractive index 1.45).<sup>24</sup>  
142 Due to the topographical aspects potentially affecting contact with the IRE, the spectra were  
143 not corrected for wavelength dependent penetration depth.

144

#### 145 *Statistical analysis*

146 Error bars were representative of the standard deviation or  $\pm 5\%$  error. One-way  
147 analysis of variance (ANOVA) followed by Newman-Keuls tests were performed using R.  
148 3.4.1 software. Differences between samples were considered statistically significant for  $p$   
149 values  $< 0.05$ .

150

#### 151 *Principal component analysis (PCA)*

152 PCA was carried out on the ATR-FTIR data measured using R (version 3.2.2, R Core  
153 Team, 2015)<sup>25</sup> and R Studio (version 0.99.486, R Studio Team).<sup>26</sup> PCA analysis was performed  
154 using the `prcomp` function as part of the `stats` package by singular value decomposition of the  
155 centred and scaled data matrix.<sup>25</sup> Results of this analysis were visualised using the `factoextra`  
156 package (version 1.0.5) and `ggplot2`.<sup>27</sup>

157

#### 158 *Partial least squares regression (PLSR)*

159 PLSR was carried out on the ATR-FTIR data using R (version 3.2.2, R Core Team,  
160 2015)<sup>25</sup> and R Studio (version 0.99.486, R Studio Team, 2015).<sup>26</sup> PLSR analysis was performed  
161 using the `pls` function as part of the `pls` package (version 2.7-1).<sup>28</sup> The kernel algorithm was  
162 used on a mean-centred predictor and response data matrix. Leave-one-out cross-validation  
163 was utilised to optimise the number of components (8) to be used in the final model.

164

## 165 **RESULTS**

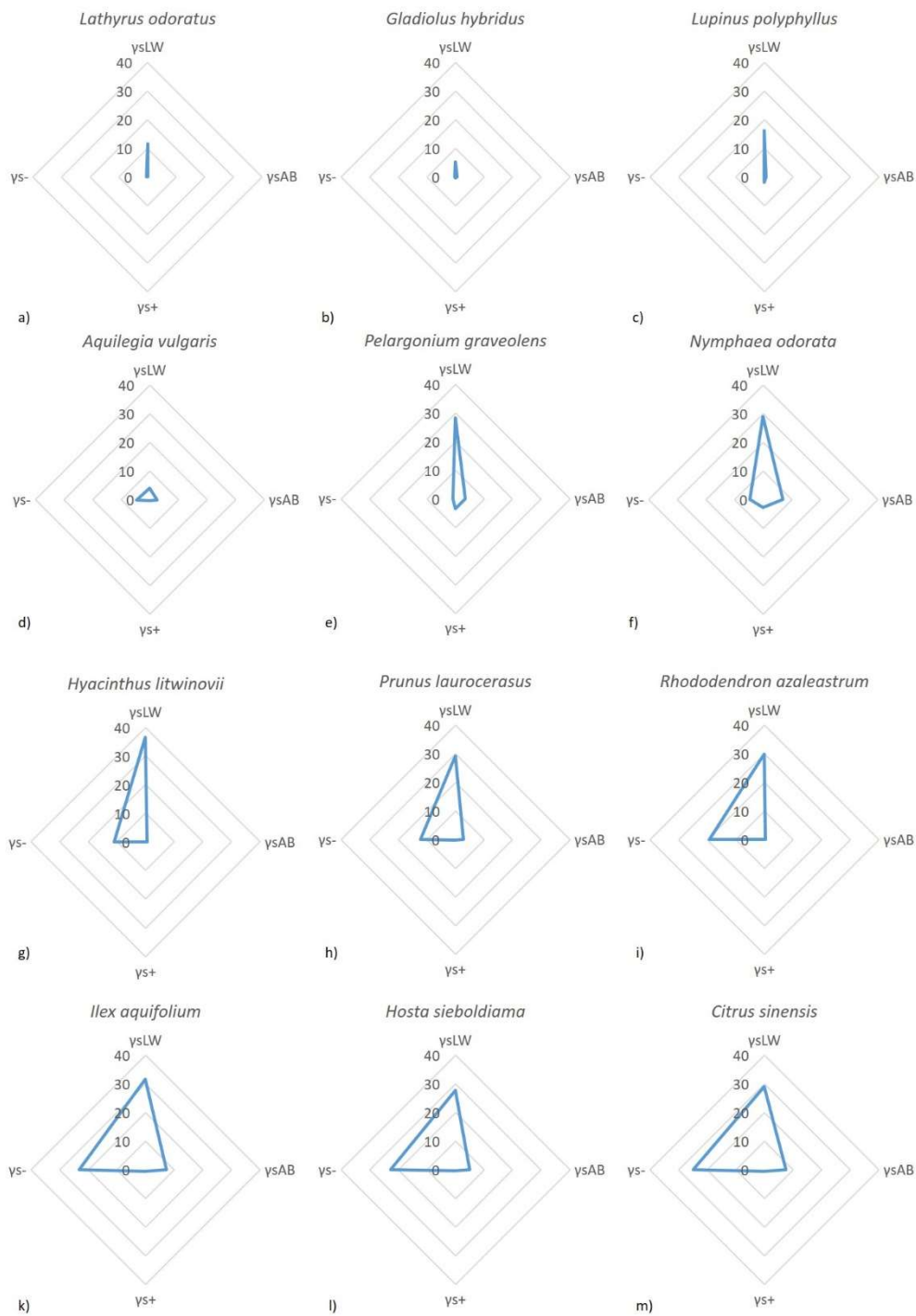
### 166 *Physicochemical properties of the leaf surfaces*

167 The physicochemical parameter values are represented in radar graphs (Figure 1) to  
168 provide a physicochemical map for each leaf surface. Furthermore, the physicochemical

169 parameters of the twelve leaf surfaces are presented in Table 1. The  $\gamma_s^{LW}$  values of all the leaves  
170 were higher than their corresponding  $\gamma_s^{AB}$  values. Therefore, all the leaves investigated had  
171 non-polar adaxial surfaces. The three most hydrophobic leaves (*Gladiolus hybridus*, *Lupinus*  
172 *polyphyllus*, and *Lathyrus odoratus*) demonstrated high  $\gamma_s^{LW}$  values and substantially lower  
173  $\gamma_s^{AB}$ ,  $\gamma_s^+$ , and  $\gamma_s^-$  values. These patterns were represented in the graphs in Figure 1 by thin  
174 asymmetric diamond shapes with the long arm pointing upwards. The base and short downward  
175 arm of the diamond was formed from the relatively insignificant  $\gamma_s^{AB}$ ,  $\gamma_s^+$ , and  $\gamma_s^-$  contributions  
176 to the total surface energy. The less hydrophobic surfaces had higher  $\gamma_s^-$  values which led to  
177 graphs with wider bases and various triangular shapes.

178





179

180 **Figure 1.** Radar graphs showing the magnitude of the surface energy components for each leaf

181 type.

182

183 **Table 1.** Physicochemical parameters of the adaxial surface of the leaf samples. The values are  
 184 expressed in  $\text{mJ/m}^2$  and the errors are in parenthesis.

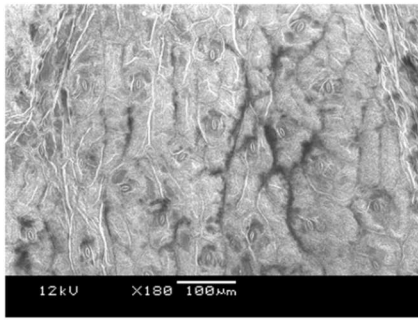
Leaf	$\Delta G_{\text{iwi}}$	$\gamma_{\text{s}}$	$\gamma_{\text{s}}^{\text{LW}}$	$\gamma_{\text{s}}^{\text{AB}}$	$\gamma_{\text{s}}^+$	$\gamma_{\text{s}}^-$
<i>Lathyrus odoratus</i>	-91.7 (9.4)	11.6 (1.0)	11.6 (0.9)	0.1 (0.3)	0.0 (0.0)	0.38 (0.43)
<i>Gladiolus hybridus</i>	-91.3 (12.2)	6.0 (1.2)	5.4 (1.0)	0.6 (0.7)	0.4 (0.4)	0.25 (0.44)
<i>Lupinus polyphyllus</i>	-74.7 (10.6)	16.4 (1.4)	16.2 (0.7)	0.2 (1.2)	1.8 (0.7)	0.00 (0.06)
<i>Aquilegia vulgaris</i>	-64.2 (16.4)	6.9 (2.1)	4.2 (1.0)	2.7 (1.8)	0.4 (0.4)	4.9 (2.90)
<i>Pelargonium graveolens</i>	-54.0 (7.9)	31.5 (1.5)	28.1 (0.9)	3.4 (1.2)	3.3 (0.7)	0.9 (0.57)
<i>Nymphaea odorata</i>	-41.1 (6.5)	35.9 (1.3)	29.0 (0.9)	6.9 (1.0)	2.6 (0.5)	4.5 (1.01)
<i>Hyacinthus litwinovii</i>	-38.3 (7.9)	37.1 (1.4)	36.6 (0.6)	0.5 (1.3)	0.0 (0.0)	10.9 (1.97)
<i>Prunus laurocerasus</i>	-30.1 (6.8)	32.0 (1.2)	29.1 (0.6)	2.8 (1.1)	0.2 (0.1)	12.2 (1.91)
<i>Rhododendron azaleastrum</i>	-14.5 (11.1)	30.3 (2.3)	29.9 (0.6)	0.4 (2.2)	0.0 (0.0)	19.3 (3.76)
<i>Ilex aquifolium</i>	-6.0 (10.5)	38.8 (2.2)	31.5 (0.6)	7.3 (2.1)	0.6 (0.3)	23.1 (3.98)
<i>Hosta sieboldiana</i>	-5.7 (32.6)	32.6 (2.8)	27.6 (1.2)	5.0 (2.6)	0.3 (0.3)	22.8 (3.50)
<i>Citrus sinensis</i>	-2.3 (10.2)	36.4 (2.2)	29.0 (0.6)	7.5 (2.1)	0.6 (0.3)	24.8 (3.99)

185

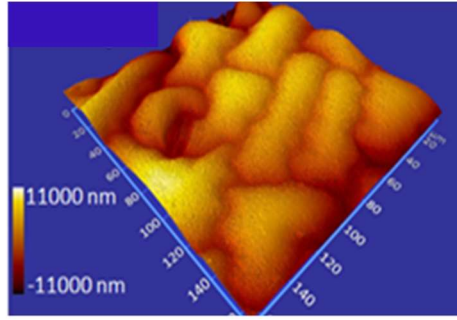
186 *Surface topography*

187 The topographies of the leaves were investigated at the macro, micro, and nanoscale scale to  
 188 comprehensively analyse the morphology of the surface features. Low magnification SEM  
 189 images (Figure 2) revealed that the macro topographies of the leaves were most commonly  
 190 characterised by platelet-type features (Figure 2a, g, j, m, p, s, ee, and hh). However, some  
 191 exhibited quite different surface topographies including homogenous distributions of raised  
 192 nodules (Figure 2d), subtle network structures (Figure 2v and y), and very flat, almost  
 193 featureless surfaces (Figure 2bb). Optical profilometry images highlighted the micro  
 194 topographies of the leaf surfaces and revealed more detailed information regarding the varied

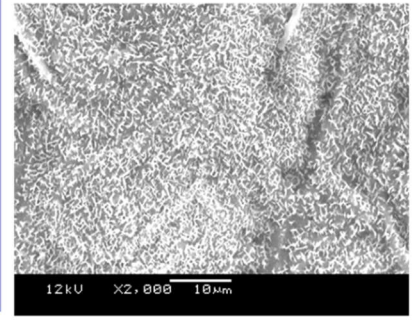
195 platelet-like morphology. For example, the average platelet feature length ranged from 10 to  
196 45  $\mu\text{m}$  and some were very regular in shape (Figure 2h, n, and ff), whilst other were far more  
197 irregular (Figure 2b, k, t, and ii). The nano features of the surface topographies were  
198 investigated using high magnification SEM. The images demonstrated that wax nanocrystals  
199 were present on all the leaf surfaces in varying amounts. The most hydrophobic surfaces  
200 (Figure 2c, 2f, 2i, and 2l) exhibited dense distributions of wax nanocrystals, whilst the less  
201 hydrophobic surfaces had far smaller amounts (Figure 2x, aa, dd, gg, and jj).  
202



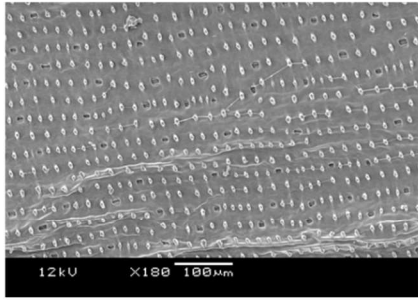
a) *Lathyrus odoratus*



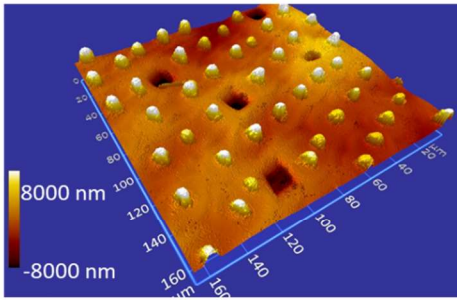
b)



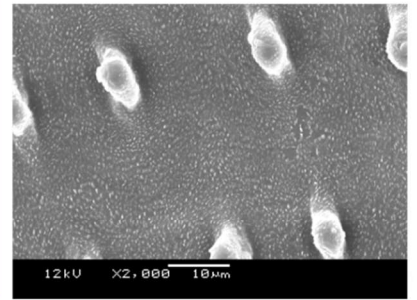
c)



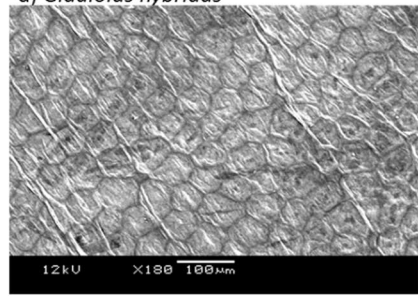
d) *Gladiolus hybridus*



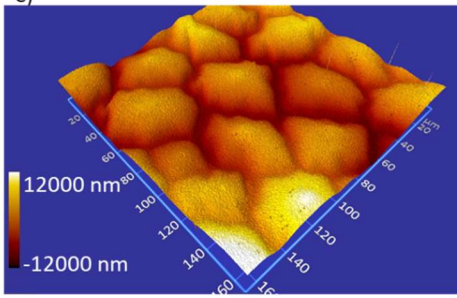
e)



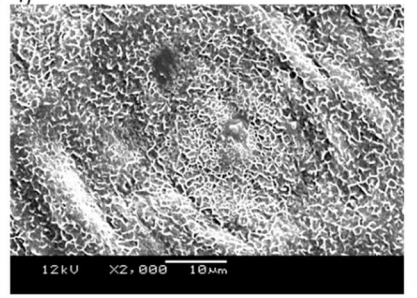
f)



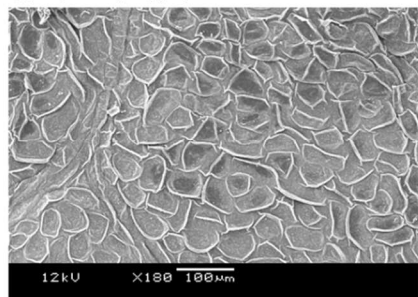
g) *Lupinus polyphyllus*



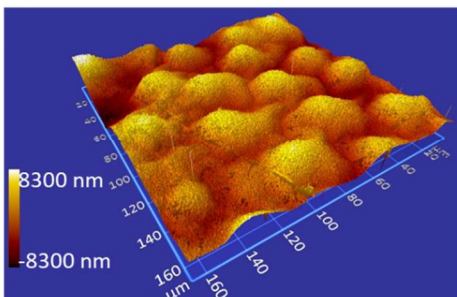
h)



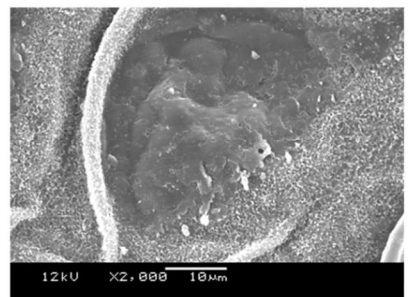
i)



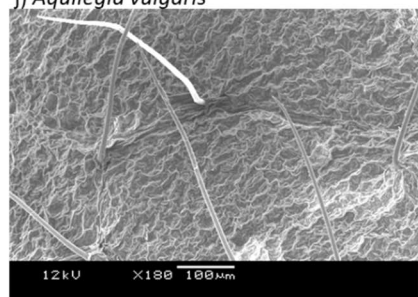
j) *Aquilegia vulgaris*



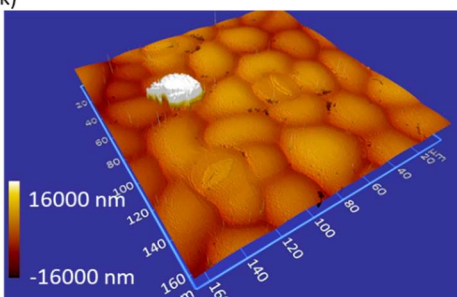
k)



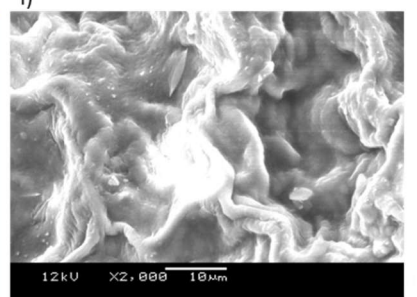
l)



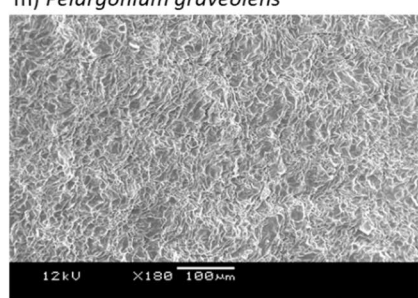
m) *Pelargonium graveolens*



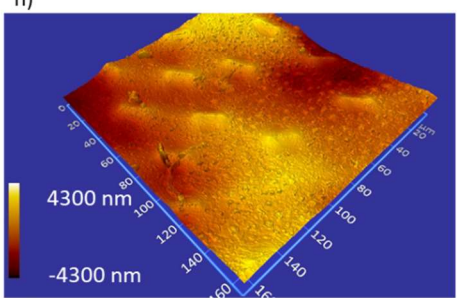
n)



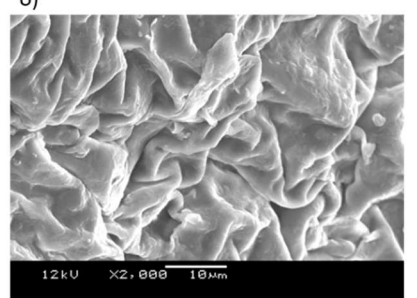
o)



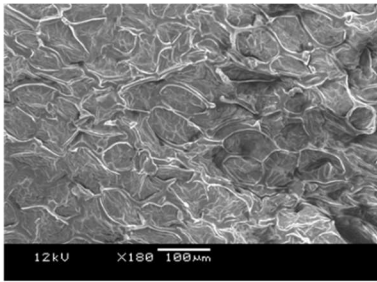
p) *Nymphaea odorata*



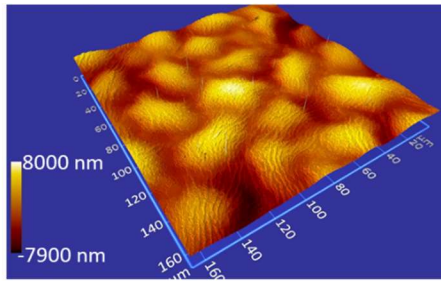
q)



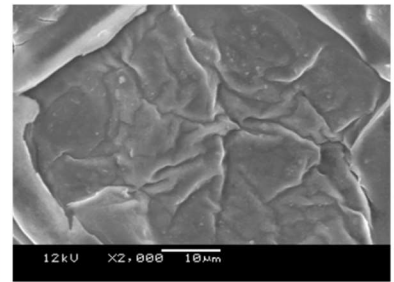
r)



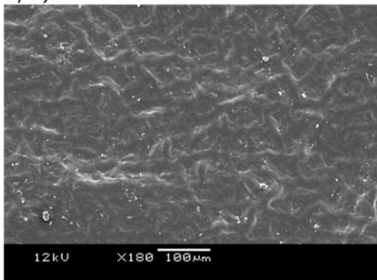
s) *Hyacinthus litwinovii*



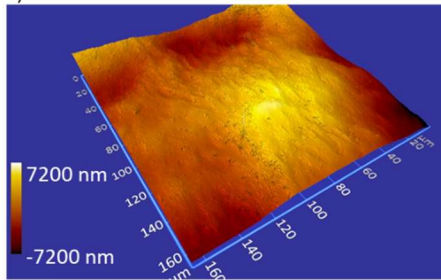
t)



u)



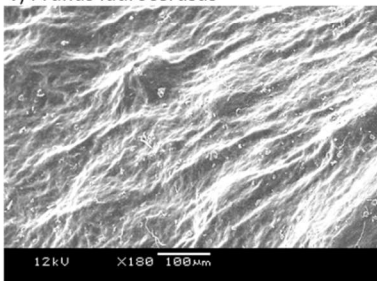
v) *Prunus laurocerasus*



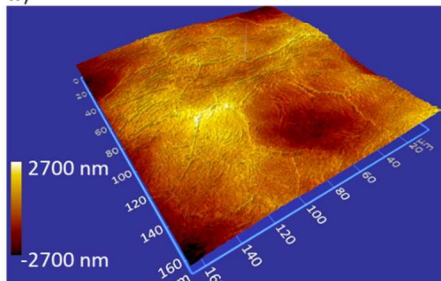
w)



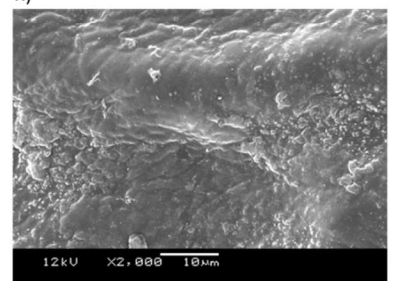
x)



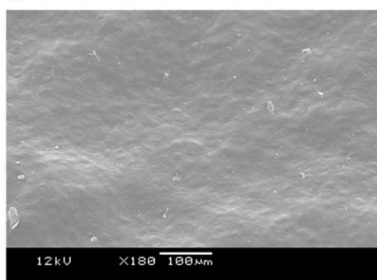
y) *Rhododendron azaleastrum*



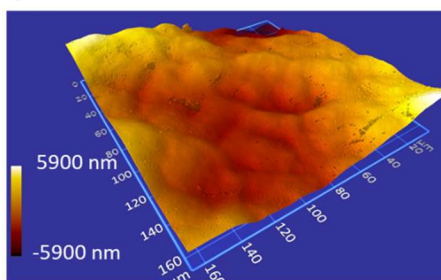
z)



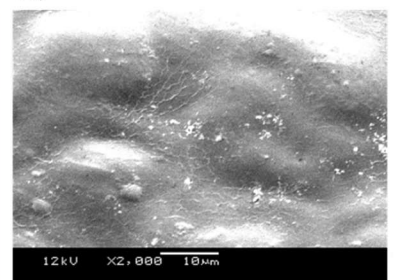
aa)



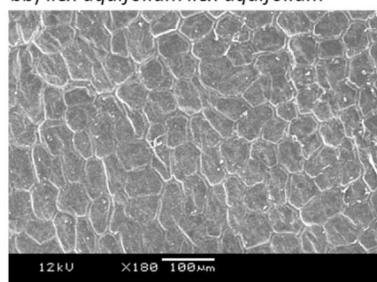
bb) *Ilex aquifolium Ilex aquifolium*



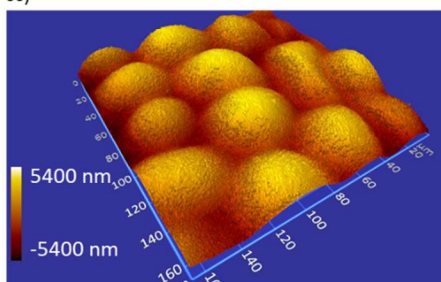
cc)



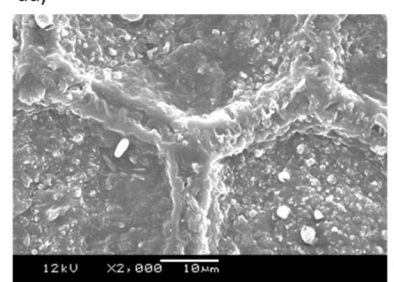
dd)



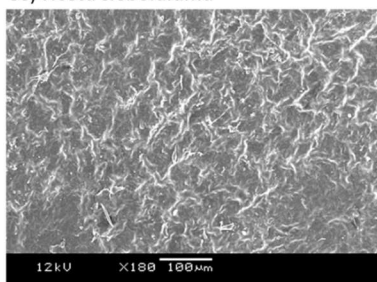
ee) *Hosta sieboldiana*



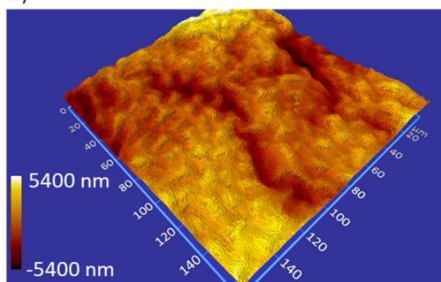
ff)



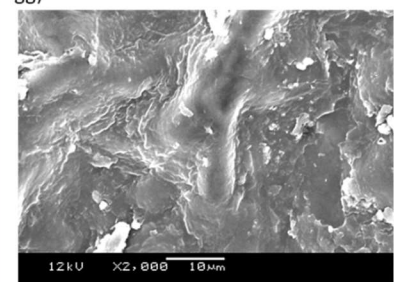
gg)



hh) *Citrus sinensis*



ii)



jj)

205 **Figure 2.** Optical profilometry and SEM images of the adaxial surfaces of the leaf samples  
 206 demonstrating their macro, micro, and nano surface topographies.

207

208 Table 3 presents the surface roughness values for each leaf type. The results demonstrate that  
 209 the more hydrophobic surfaces generally had the greatest roughness values, whilst the least  
 210 hydrophobic surfaces had the lowest roughness values. However, there were some exceptions  
 211 to this trend. For example, the *Pelargonium graveolens* had the largest roughness values.  
 212 Similarly, the *Hyacinthus litwinovii* leaf, which was not one of the most hydrophobic surfaces,  
 213 also had large  $S_a$  (2.8  $\mu\text{m}$ ) and  $S_{pv}$  (118.9  $\mu\text{m}$ ) values. Generally, the least hydrophobic surfaces  
 214 had less defined surface features. The exception was the *Hosta sieboldiana*, which had low  
 215 surface roughness values but still demonstrated defined platelet-type features on its surface  
 216 (Figure 2n).

217

218 **Table 3.** Surface roughness parameters of the leaf samples obtained from the optical  
 219 profilometry data. The standard deviations are indicated in parenthesis.

Leaf	$S_a$ ( $\mu\text{m}$ )	$S_q$ ( $\mu\text{m}$ )	$S_{pv}$ ( $\mu\text{m}$ )
<i>Lathyrus odoratus</i>	3.2 (0.6)	3.9 (0.7)	36.5 (8.5)
<i>Gladiolus hybridus</i>	2.6 (0.9)	3.6 (1.1)	69.2 (20.1)
<i>Lupinus polyphyllus</i>	4.3 (1.4)	5.3 (1.8)	41.1 (10.1)
<i>Aquilegia vulgaris</i>	2.9 (0.4)	3.6 (0.6)	41.5 (8.1)
<i>Pelargonium graveolens</i>	5.9 (1.5)	9.4 (2.0)	148.2 (15.2)
<i>Nymphaea odorata</i>	0.8 (0.1)	1.1 (0.2)	9.9 (3.0)
<i>Hyacinthus litwinovii</i>	2.8 (0.9)	3.5 (1.2)	118.9 (19.2)
<i>Prunus laurocerasus</i>	2.0 (0.4)	2.4 (0.4)	13.4 (2.8)
<i>Rhododendron azaleastrum</i>	2.2 (1.1)	2.9 (1.5)	40.0 (21.4)

<i>Ilex aquifolium</i>	1.2 (0.2)	1.4 (0.2)	9.0 (2.0)
<i>Hosta sieboldiana</i>	2.0 (0.4)	2.5 (0.5)	28.8 (11.5)
<i>Citrus sinensis</i>	1.6 (0.4)	2.1 (0.5)	31.9 (18.6)

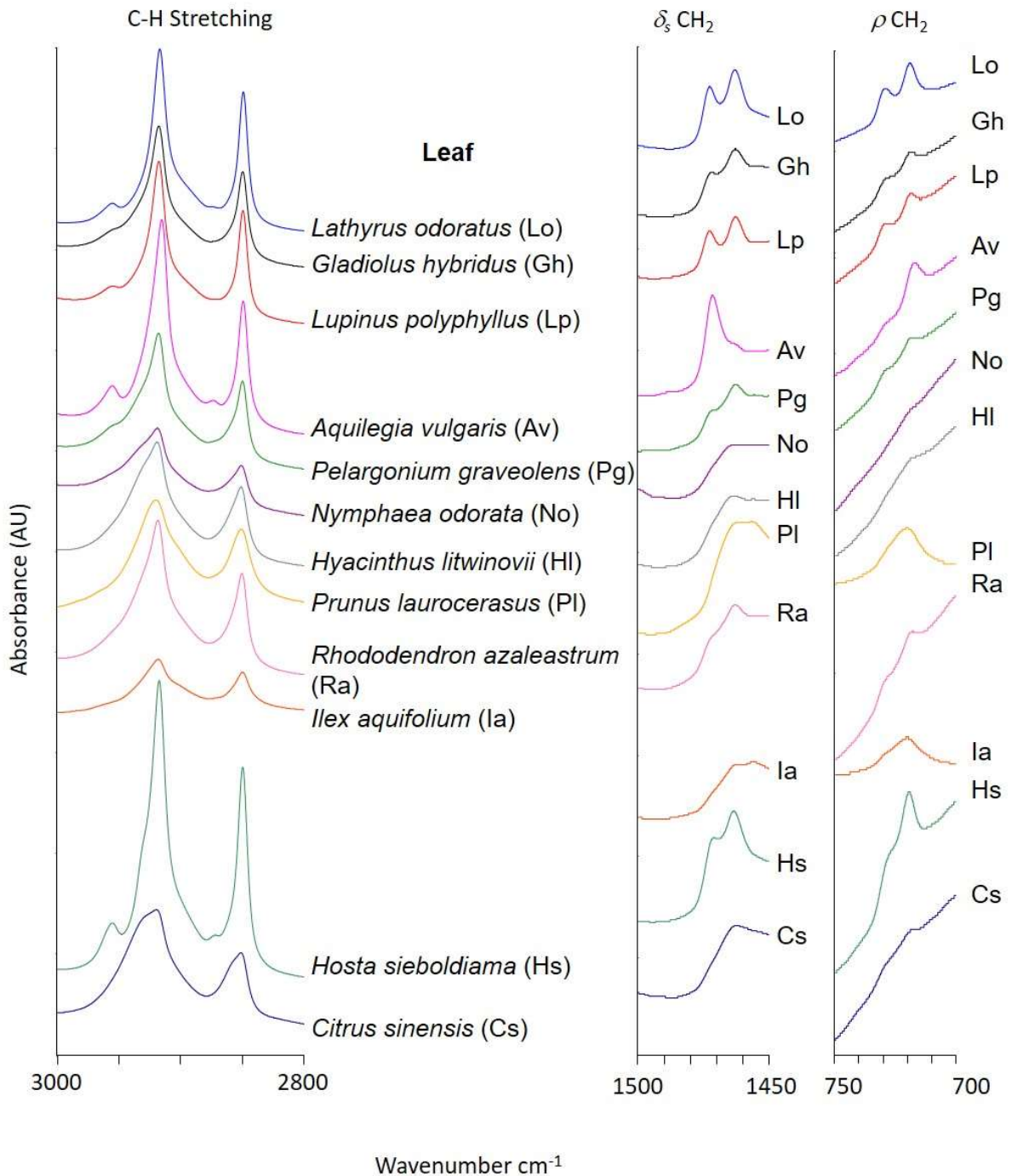
---

220

221 *Surface chemistry*

222 ATR-FTIR was used to identify the major classes of chemical species within the first  
223 few microns of the adaxial surfaces of the leaves (Figures 3 and 4). All the leaf spectra generally  
224 featured a relatively strong and broad hydrogen-bonded OH stretching band centred at 3300  
225  $\text{cm}^{-1}$  (Peak A, Figure 3). For the *Prunus laurocerasus* and *Hosta sieboldiana*, this band was  
226 noticeably weak relative to the C-H stretching bands (centred at ca. 2900  $\text{cm}^{-1}$ ). However, for  
227 the *Nymphaea odorata*, the OH band was more intense than the C-H band. The *Gladiolus*  
228 *hybridus*, *Citrus sinensis*, *Hyacinthus litwinovii*, and *Pelargonium graveolens* leaves had an  
229 OH band that was of near equal intensity to the C-H band. The OH band can be assigned to  
230 alcohols, carboxylic acids, and water. All the leaves exhibited two bands at 2916 and 2846  $\text{cm}^{-1}$   
231 <sup>1</sup> (asymmetric ( $\nu_{as}$  CH<sub>2</sub>) and symmetric ( $\nu_s$  CH<sub>2</sub>) methylene C-H stretching, respectively),  
232 which corresponded to the non-polar hydrocarbon compounds on their surfaces. The  
233 accompanying methylene C-H deformation (scissoring ( $\nu_s$  CH<sub>2</sub>)) and C-H rocking ( $\nu$ CH<sub>2</sub>)  
234 bands centred at ca. 1450 and 720  $\text{cm}^{-1}$ , respectively, were also evident. All the leaves featured  
235 carbonyl (C=O) bearing species that generally absorbed at 1735  $\text{cm}^{-1}$ , indicating the possible  
236 dominance of ester-based compounds present in the leaf composition. A broad collection of  
237 bands centred at ca. 1630  $\text{cm}^{-1}$  was also evident on all the leaves which can be assigned mainly  
238 to H-O bending modes of the water molecule. In all cases, except *Hosta sieboldiana* and to a  
239 lesser extent *Prunus laurocerasus*, the absorbance of this band was indicative of the OH  
240 stretching band. In the exceptional cases of *Hosta sieboldiana* and *Prunus laurocerasus*, there  
241 was significant confounding with other chemical species that absorbed in the same region. For

242 *Hosta sieboldiana*, there was a strong and sharp band ( $1640\text{ cm}^{-1}$ ) in this region. For all the  
 243 leaf surfaces, a band at  $1055\text{ cm}^{-1}$  was detected which could correspond to the C–O stretching  
 244 of primary alcohols that are present.

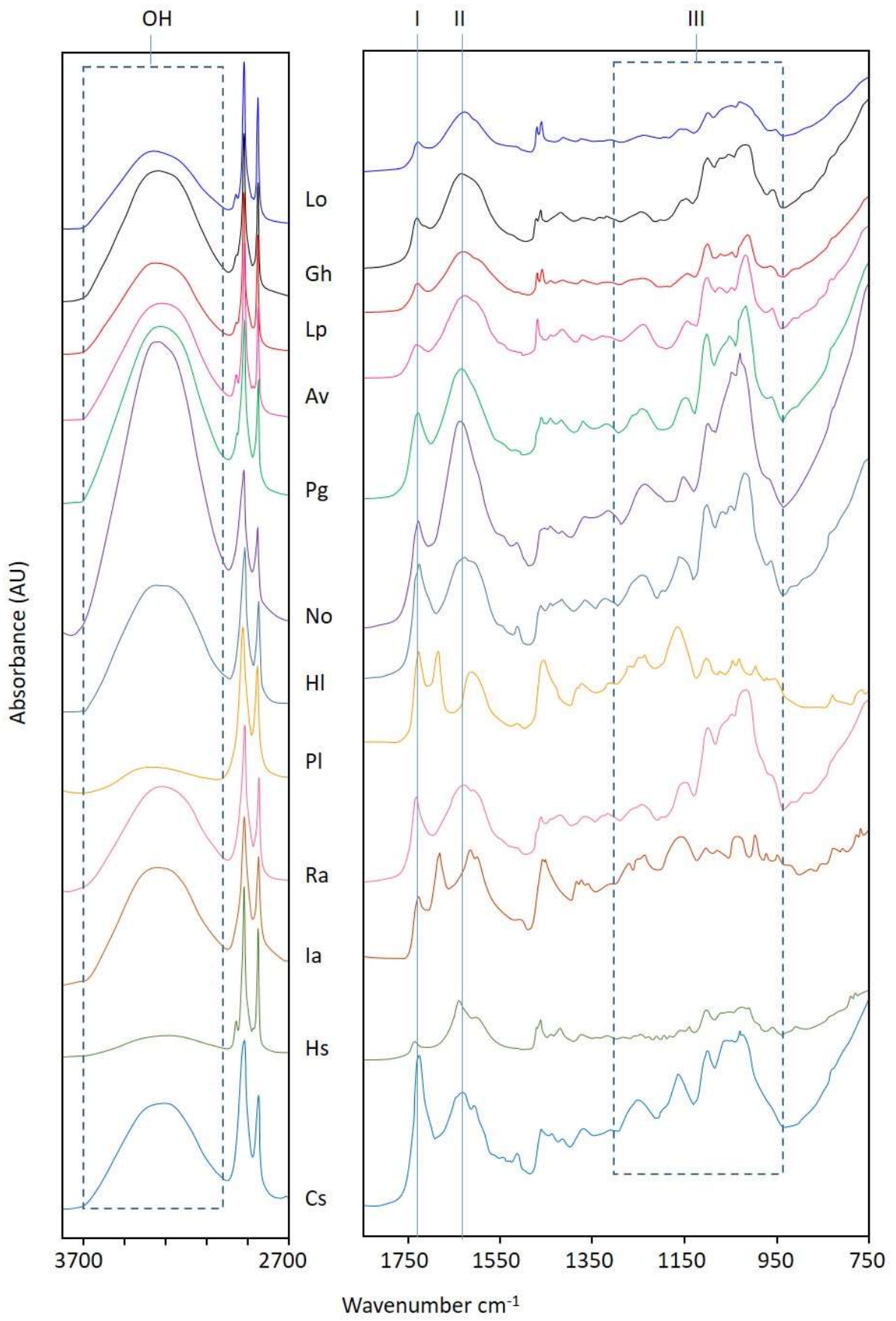


245  
 246 **Figure 3.** ATR-FTIR spectra showing OH and CH stretching and fingerprint regions of the  
 247 leaf surfaces. Note that absorbance has been normalised to the C-H stretching bands to  
 248 compensate for differences in effective contact area.



249

250 A band at  $1032\text{ cm}^{-1}$  was detected on the *Lathyrus odoratus*, *Nymphaea odorata*,  
251 *Hyacinthus litwinovii*, *Prunus laurocerasus*, *Ilex aquifolium*, *Hosta sieboldiana*, and *Citrus*  
252 *sinensis* leaf surfaces, which could correspond to the C–O stretching of secondary alcohols.  
253 Interestingly, pronounced splitting of the  $\nu_s\text{ CH}_2$  and  $\nu\text{CH}_2$  bands was detected in the spectra  
254 of the *Gladiolus hybridus*, *Hosta sieboldiana*, *Lupinus polyphyllus*, and *Lathyrus odoratus*,  
255 which can be assigned to the presence of highly crystalline wax structures (Figure 4). This was  
256 also evident on the *Aquilegia vulgaris* and *Pelargonium graveolens* leaf surfaces but to a lesser  
257 extent. The *Ilex aquifolium* and *Prunus laurocerasus* surfaces exhibited a single  $\nu\text{CH}_2$  band at  
258  $719\text{ cm}^{-1}$ , which could indicate a disordered (liquid-like) arrangement of long alkyl chains. The  
259 *Hyacinthus litwinovii* and *Nymphaea odorata* showed weak  $\nu_s\text{ CH}_2$  and  $\nu\text{ CH}_2$  bands hindering  
260 detection of splitting. The *Hosta sieboldiana* differed from the other surfaces in that it also  
261 demonstrated a  $\nu_{\alpha s}\text{ CH}_2$  band at  $2925\text{ cm}^{-1}$  and a C=O peak at  $1640\text{ cm}^{-1}$ . Overall with regards  
262 to the surface chemistries, the molecules observed on all the surfaces were those likely to be  
263 related to the cutin structure of the surface.<sup>14</sup> The results demonstrate that the main differences  
264 in the surface chemistry were related to the disordered arrangement of wax-like chains (*Prunus*  
265 *laurocerasus* and *Hosta sieboldiana*), in addition to the C=O and  $\nu_{\alpha s}\text{ CH}_2$  group of the *Hosta*  
266 *sieboldiana*.



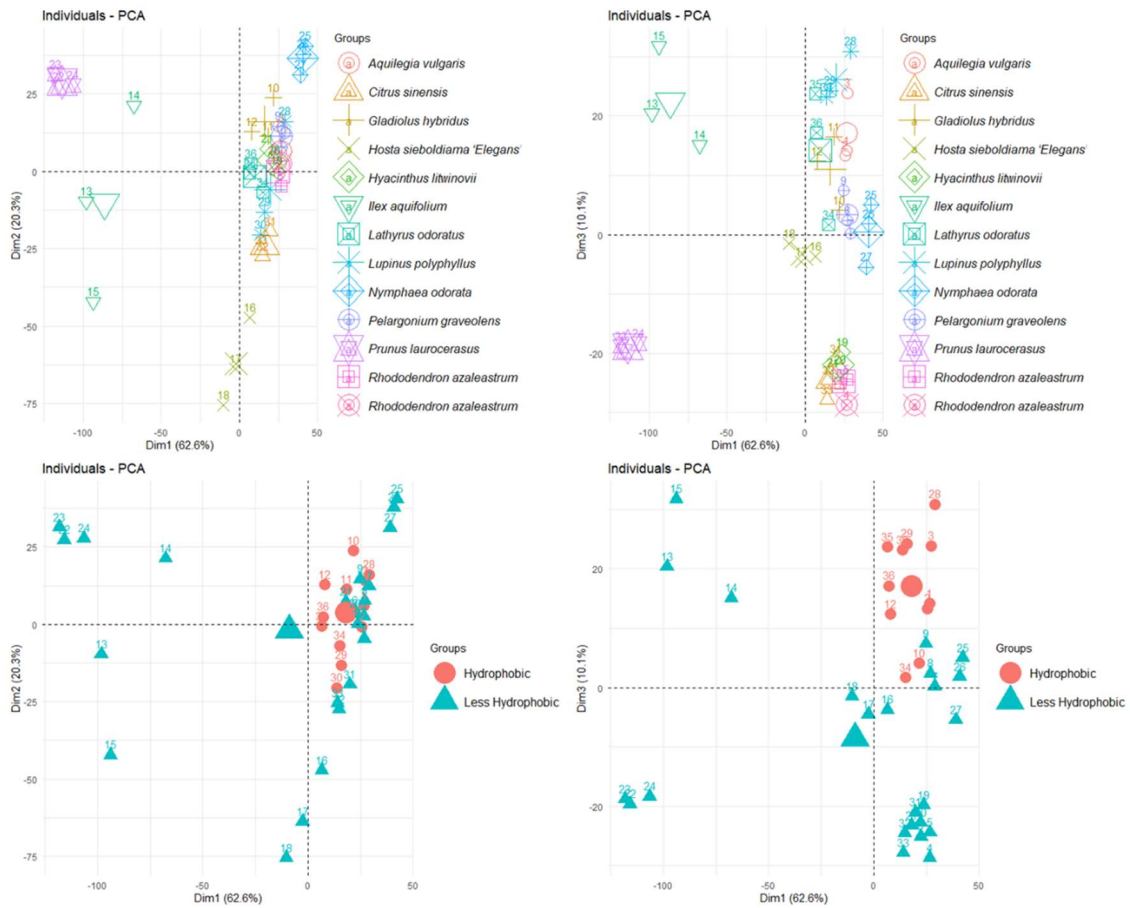
268 **Figure 4.** C-H stretching, C-H deformation, and C-H rocking regions of the ATR-FTIR spectra  
269 of the leaf samples showing variations in hydrocarbon content and structural ordering of wax  
270 components (splitting of the  $\nu_s$  CH<sub>2</sub> and  $\nu$ CH<sub>2</sub> bands). Band I: carbonyl stretching from esters  
271 and other carbonyl compounds; Band II: assigned to the H-OH bending vibration of water;  
272 Bands III: various C-O stretching and C-N stretching vibrations. Lo: *Lathyrus odoratus*, Gh:  
273 *Gladiolus hybridus*, Lp: *Lupinus polyphyllus*, Av: *Aquilegia vulgaris*, Pg: *Pelargonium*  
274 *graveolens*, No: *Nymphaea odorata*, Hl: *Hyacinthus litwinovii*, Pl: *Prunus laurocerasus*, Ra:  
275 *Rhododendron azaleastrum*, Ia: *Ilex aquifolium*, Hs: *Hosta sieboldiana*, Cs: *Citrus sinensis*.

276

#### 277 *PCA and PLSR modelling of surface chemistry data*

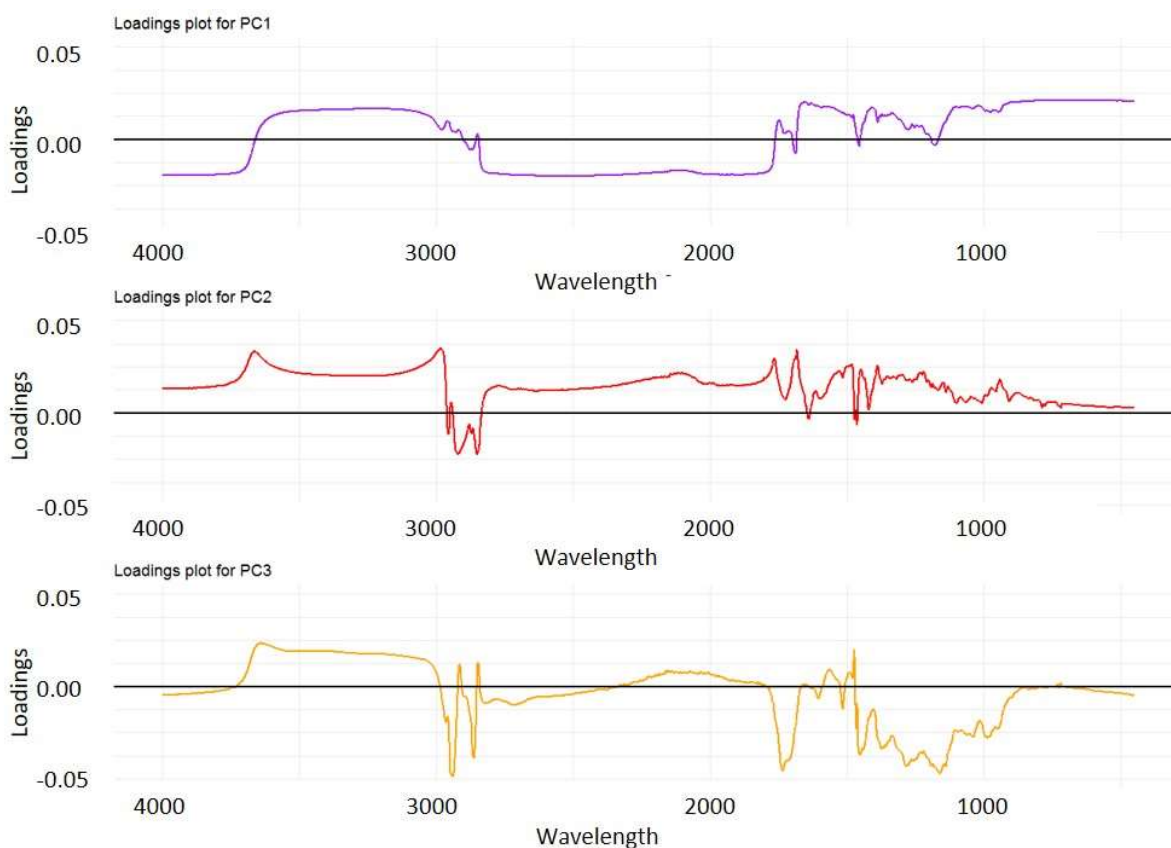
278 The ATR-FTIR spectral data provided a basis for further statistical analysis of the  
279 leaves. PCA was performed to analyse the results of the ATR-FTIR measurements to provide  
280 a greater understanding of the relationships between the variables within the data.<sup>29</sup> The PCA  
281 data is presented using score plots labelled by leaf type on the top and class (i.e level of  
282 hydrophobicity) on the bottom (Figure 5), in addition to the loading plots of the first three  
283 principal components (Figure 6). Analysing the loading plots (Figure 6) for each of the  
284 principal components enabled the determination of which section(s)/peaks of the ATR-FTIR  
285 spectra were influential in the relative positioning of the leaves in PCA and could be used to  
286 relate back to the original spectra. Additionally, analysing the PCA when categorising the  
287 samples according to their classification (surface wettability) revealed that the most  
288 hydrophobic leaves shared common surface chemistry traits, demonstrated by being grouped  
289 in close proximity with low intra-class variability (Figure 5, bottom). Based on their placement  
290 in principal component 1 (PC1), it was concluded that the most hydrophobic leaves had strong  
291 peaks pertaining to the OH stretching band, which could be observed when analysing the raw  
292 data (Figure 5, bottom). The hydrophobic leaves also exhibited strong asymmetric ( $\nu_{as}$  CH<sub>2</sub>)

293 and symmetric ( $\nu_s$  CH<sub>2</sub>) methylene C-H stretching peaks at  $\sim 2916$  and  $\sim 2846$  cm<sup>-1</sup>,  
294 respectively, in addition to weak carbonyl ester peaks at  $\sim 1735$  cm<sup>-1</sup>. Furthermore, one of the  
295 peaks that was a unique contributor to principal component 3 (PC3) included the split CH<sub>2</sub> peak  
296 ( $\sim 1475$  cm<sup>-1</sup>) methylene asymmetric ( $\nu_{as}$  CH<sub>2</sub>) C-H deformation which was only present in the  
297 most hydrophobic leaves. This peak is indicative of non-cutin wax structures. In contrast, the  
298 least hydrophobic leaves have highly-variable surface chemistry as measured by ATR-FTIR,  
299 demonstrated by their scattered positions in the score plots. Interestingly, with the exception of  
300 a few of the leaf samples, the hydrophobic and less-hydrophobic classified leaves could almost  
301 be completely separated on the basis of their position according to PC3. This indicated that the  
302 characteristics that contributed to this principal component could be used to distinguish  
303 between these classifications and that their profile/values for these bands and corresponding  
304 functional groups were very important in determining the hydrophobicity of a surface.



305

306 **Figure 5.** Score plots labelled by leaf type (top) and class, i.e. hydrophobicity, (bottom) of PC1  
 307 vs PC2 (left) and PC1 vs PC3 (right) for the PCA of the ATR-FTIR spectra.



308  
 309 **Figure 6.** Loading plots for the PCA of the ATR-FTIR spectra of the first three PCs. PC1 (top),  
 310 PC2 (middle), and PC3 (bottom).

311  
 312 Assessing the data by leaf type, it was clear that the ATR-FTIR of *Prunus laurocerasus*  
 313 and *Ilex aquifolium* were very distinct from each other, as well as the other leaves in terms of  
 314 the components that contribute to PC1 (Figure 5, top). Additionally, the *Hosta sieboldiana*  
 315 was different from the other leaves ( $\nu_{as}$  CH<sub>2</sub>, C=O) that contributed to PC2. On determination  
 316 of which areas of the ATR-FTIR spectra had distinct loadings for PC2 compared to the other  
 317 PCs, it was observed that PC2 featured (among others) peaks at 2925 and 1640 cm<sup>-1</sup>  
 318 (downwards), and was the only PC that had notable influence by peaks in the 800-650 cm<sup>-1</sup>  
 319 range (Figure 6 middle). In contrast to the other leaf samples, *Hosta sieboldiana* exhibited a  
 320 notable peak centred at ~2925 cm<sup>-1</sup> shouldering the  $\nu_s$  CH<sub>2</sub> band (ca. 2916 cm<sup>-1</sup>) and was the  
 321 only leaf to exhibit a sharp absorption at 1640 cm<sup>-1</sup>. Furthermore, the *Hosta sieboldiana* leaves

322 showed a very strong peak in the C-H rocking ( $\nu\text{CH}_2$ ) region at  $\sim 720\text{ cm}^{-1}$ , an area that also  
323 influences PC2 and further accounts for its marked positioning in PC2 away from other leaves.

324 While differences in various methylene frequencies were largely demonstrated by PC2,  
325 the broad hydrogen bonded OH stretching band centred at  $3300\text{ cm}^{-1}$  was a main contributor to  
326 PC1 (Figure 6, top). As such, the positioning of the species along the horizontal axes of all the  
327 score plots in Figure 5, representing PC1, was demonstrative of the strength of this peak. As  
328 aforementioned, this peak was very weak for *Prunus laurocerasus* which explains its leftmost  
329 position in the PCA score plots. Furthermore, this peak was also weak for the *Ilex aquifolium*  
330 and *Hosta sieboldiana*, and thus they were also positioned on the left side in PC1. In contrast,  
331 the *Nymphaea odorata* had the most prominent OH stretching band, accounting for its  
332 rightmost positioning in PC1. The H-O bending modes at ca.  $1630\text{ cm}^{-1}$  also contributed to  
333 PC1, with lower intensity peaks differentiating *Prunus laurocerasus* and *Ilex aquifolium* from  
334 the other samples. It can be surmised that PC1 was mostly influenced by ATR-FTIR peaks  
335 attributable to O-H bands (stretching  $\sim 3300$  and  $1630\text{ cm}^{-1}$ ), while PC2 was most influenced  
336 by C-H methylene-related bands.

337 In addition to the PCA, further statistical analysis was performed using PLSR to model  
338 the leaves WCA, and hence their surface wettability from the ATR-FTIR measurements. To  
339 the authors knowledge, this was the first time that such a model has been implemented on a  
340 complex biological system, whereby an attempt using such a system was used to determine if  
341 it was possible to relate surface chemistry and WCA. It was found that the PLSR model was  
342 able to account for  $\sim 95\%$  of the variation in WCA with eight components. This showed that  
343 extremely variable data was able to be explained by the developed model, indicating a high  
344 level of applicability of such a system to analyse complex data. Analysing the loading plot  
345 (Figure S1) for the first three principal components for the model (PC1, 85%, black solid line;  
346 PC2, 8%, red dashed line and PC3, 5%, green dotted line), observations could be made about

347 the influence of various bands in the ATR-FTIR spectra that were most influential to this  
348 model, in relation to the WCA of the leaf surface. As seen following PCA, PC1 for this model  
349 was strongly influenced by the prominent OH stretching band centred at  $3300\text{ cm}^{-1}$ , whilst PC2  
350 was largely influenced by this peak but also the asymmetric and symmetric methylene  $\text{CH}_2$  C-  
351 H stretching peaks at  $\sim 2916\text{ cm}^{-1}$  and  $\sim 2846\text{ cm}^{-1}$ , respectively. These bands within the loading  
352 plots were the main contributors to these principal components which attests to their  
353 importance and influence on the WCAs. Validation of the resulting regression model from this  
354 analysis indicated very good correlation ( $R^2 = 0.86$ ) between measured and predicted values,  
355 indicating its potential for predicting surface hydrophobicity from ATR-FTIR spectra of a  
356 given surface (see Figure S2 for the plot depicting the performance of the PLSR model).

357

## 358 DISCUSSION

359 Overall, there were some clear demarcations in the surface properties and composition  
360 of the leaf samples. The *Lathyrus odoratus*, *Gladiolus hybridus*, and *Lupinus polyphyllus* were  
361 the most hydrophobic with  $\Delta G_{\text{iwi}}$  values of  $-91.7$ ,  $-91.3$ , and  $-74.7\text{ mJ/m}^2$ , respectively. Their  
362 surface properties fitted with the Cassie-Baxter model of self-cleaning surfaces and they shared  
363 common traits such as high  $S_a$ ,  $S_q$ , and  $S_{pv}$  values, and low  $\gamma_s^{\text{LW}}$ ,  $\gamma_s^{\text{AB}}$ , and  $\gamma_s^-$  components.  
364 However, the surface topography of the *Lathyrus odoratus* and *Lupinus polyphyllus* was  
365 characterised by platelet-like features, whereas the *Gladiolus hybridus* surface was populated  
366 by a homogenous distribution of raised nodules. The presence of wax nanocrystals was also  
367 evident on all three surfaces. Furthermore, their ATR-FTIR spectra exhibited splitting of the  $\nu_s$   
368  $\text{CH}_2$  and  $\nu\text{CH}_2$  bands. This indicated hydrocarbon wax crystallisation, which was in agreement  
369 with the SEM images that showed distinct wax crystallisation on their surfaces. Thus, it  
370 appeared that a high degree of surface roughness and the presence of a dense population of wax  
371 nanocrystals corresponded to a very hydrophobic leaf surface. However, it did not appear that



372 the shape of the surface features distinctly influenced its hydrophobicity. This fits with the  
373 Cassie-Baxter model whereby air (or gas) pockets may be trapped in the cavities of a rough  
374 surface, resulting in a hydrophobic surface due to a composite interface with air pockets trapped  
375 under the droplet.<sup>30</sup> It has also been suggested that nanoroughness is required to support  
376 nanodroplets.<sup>31,32</sup> Thus, it might be likely that an interplay of all these factors resulted in the  
377 most hydrophobic surfaces, although the exact parameters that impact this effect are still  
378 unclear.

379 The *Aquilegia vulgaris* was the fourth most hydrophobic surface and had greater  $\gamma_s^{AB}$   
380 and  $\gamma_s^-$  components, as well as less splitting of the  $\nu_s \text{CH}_2$  and  $\nu \text{CH}_2$  bands compared to the  
381 three most hydrophobic leaves. The *Pelargonium graveolens* was the fifth most hydrophobic  
382 surface and the only one with distinct trichomes. The *Pelargonium graveolens* had higher  $\gamma_s^{LW}$ ,  
383  $\gamma_s^{AB}$ , and  $\gamma_s^+$  components than the four most hydrophobic surfaces which is likely influenced by  
384 the trichomes on its surface. Godeau et al.<sup>33</sup> observed that the trichomes on *Echeveria pulvinata*  
385 leaves were hydrophobic, whilst the surface from which the trichomes protruded was  
386 hydrophilic. Water droplets may also rest on the trichomes as perfect spheres which means they  
387 can easily run off the leaves.<sup>1</sup>

388 The surfaces with intermediate hydrophobicity (*Nymphaea odorata*, *Hyacinthus*  
389 *litwinovii*, *Prunus laurocerasus*, and *Rhododendron azaleastrum*) had mostly featureless  
390 topographies, with the exception of the *Hyacinthus litwinovii* (platelet-like features).  
391 Furthermore, there were no clear trends in their surface roughness or physicochemical values.  
392 From the analysis, it was expected that the *Nymphaea odorata* would have been more  
393 hydrophobic. However, the *Nymphaea odorata* surfaces used in this work had very few  
394 topographical features. Additionally, compared to the other leaves, the *Nymphaea odorata*  
395 surface exhibited intense OH stretching bands in the ATR-FTIR results, which would render  
396 the surface more polar, and hence less hydrophobic. This effect may have been due to the age

397 of the leaf,<sup>2,34</sup> thus suggesting that further studies are required to determine the surfaces of  
398 leaves over time with respect to changes in their self-cleaning and water repellent properties.

399 The PCA identified the *Prunus laurocerasus* and *Ilex aquifolium* surfaces as being  
400 chemically different to the other leaves. Both these surfaces demonstrated disordered (liquid-  
401 like) arrangements of long alkyl chains which may have contributed to their differentiation in  
402 the PCA. The least hydrophobic surfaces, the *Ilex aquifolium*, *Hosta sieboldiana*, and *Citrus*  
403 *sinensis*, had the lowest  $\Delta G_{\text{iwi}}$  values of -6.0, -5.7, and -2.3 mJ/m<sup>2</sup>, respectively. These surfaces  
404 also had the highest  $\gamma_s$ ,  $\gamma_s^{\text{AB}}$ , and  $\gamma_s^-$  values. Differentiation in the surface topographies of the  
405 three least hydrophobic leaves was more complex compared to the more hydrophobic surfaces.  
406 However, the  $S_a$  and  $S_q$  values of the surfaces were generally lower than the other plant surfaces  
407 with the exception of the *Nymphaea odorata* and *Prunus laurocerasus*. Both the *Ilex*  
408 *aquifolium* and *Citrus sinensis* had surfaces with subtle features. Waxes may influence the  
409 chemical difference in the leaves, and may be detected using FTIR, even if they occur as filling  
410 material within the basic cutin network (intracuticular) rather than being present on top of the  
411 cuticle (epicuticular).<sup>35</sup>

412 The *Hosta sieboldiana* was an anomaly among the leaf samples as it exhibited distinct  
413 surface features characterised by platelet-like protrusions, but was the second most wettable  
414 surface. It also had a high  $\gamma_s^-$  value, in addition to a higher energy shoulder on the  $\nu_{\text{as}}$  CH<sub>2</sub> band  
415 and a strong sharp absorption at 1640 cm<sup>-1</sup> that was not present in any of the other spectra. This  
416 peak can be attributed to C=O carbonyl groups present, which demonstrated polar attributes.  
417 These features were further highlighted in the PCA, particularly with regard to the positioning  
418 within PC2. The ATR-FTIR spectrum of the *Hosta sieboldiana* exhibited a shoulder on the  
419 methylene C-H stretch at ~2925 cm<sup>-1</sup>, which indicated that different hydrocarbons were present  
420 in this species. This was represented in the PCA through the distinct positioning away from the  
421 other species. These hydrocarbons may be associated with polar areas that could contribute to

422 the high  $\gamma_s^-$  values. Furthermore, in the H-OH bend band, the *Hosta sieboldiama* had another  
423 absorption (1640  $\text{cm}^{-1}$ ) superimposed within the spectra, which was also accompanied by a  
424 small doublet peak at 787 and 777  $\text{cm}^{-1}$ . These peaks may be assignable to amine or amide  
425 moieties which contributed to the high  $\gamma_s^-$  values recorded. These observations are likely to be  
426 related to the presence of polar domains on the *Hosta sieboldiama* leaf, that in this case, had a  
427 dominant effect on surface hydrophobicity rather than the surface topography.

428         The leaf surfaces studied in this work exhibited a range of different properties and yet  
429 all were water repellent and self-cleaning. An elegant explanation was offered by Zhang et al.<sup>36</sup>  
430 as to why droplets on surfaces with features that are associated with the highly adhesive Wenzel  
431 state can also be self-cleaning, like those surfaces that display the typical Lotus attributes  
432 associated with the Cassie-Baxter state. It is known that on surfaces consistent with Cassie-  
433 Baxter properties, self-cleaning is achieved due to low contact angle hysteresis and small  
434 hydrodynamic resistance. Zhang et al.<sup>36</sup> further suggested that on surfaces in the Wenzel state,  
435 small neighbouring droplets can coalesce into bigger ones, and the corresponding release of  
436 surface energy results in a transition to the Cassie-Baxter state, and therefore self-cleaning  
437 action is achieved.

438         Two methods of additional statistical analysis, PCA and PLSR, were used to explore  
439 and enhance the relationship between the surface chemistry characteristics, as measured using  
440 ATR-FTIR, and the surface wettability. PCA is an excellent and powerful tool to detect any  
441 underlying clusters and groupings in the data when analysing the entire surface chemistry  
442 profile. Additionally, as this technique does not make any assumptions about the data, nor does  
443 it take into account existing classifications, any notable patterns and trends found using this  
444 unsupervised approach can be confidently surmised to exist based on the ATR-FTIR spectra,  
445 not their classification. Differences seen between sample classes (i.e. hydrophobic vs less  
446 hydrophobic surfaces and different species) and the contributing factors to those differences

447 provide insight into what distinguishes them. In our presented analysis, we were able to not  
448 only identify characteristics of hydrophobic leave surfaces and what are common features  
449 amongst leaves of this type but we were also able to identify species that were particularly  
450 unique and what about them was so discernible (i.e. *Prunus laurocerasus* and *Ilex aquifolium*).  
451 This analysis was based solely off the surface chemistry ATR-FTIR spectra and clearly  
452 demonstrates the influence surface chemistry has on the wettability of leave surfaces and it is  
453 not just the surface physicochemical properties and topography that dictate hydrophobicity of  
454 leaf surfaces.

455         Similar to PCA, the PLSR model was used to analyse the entire ATR-FTIR spectra,  
456 although this model was concerned with equating the quantitative variable, WCA, as a critical  
457 measure of surface wettability. The PLSR model found similar bands in the ATR-FTIR to be  
458 the most important at influencing surface wettability. Furthermore, the presented PLSR model  
459 showed excellent performance in validation (using a leave-one-out technique) and based on  
460 these results, it could be suggested that leaf WCA (i.e. hydrophobicity) can be predicted using  
461 ATR-FTIR surface chemistry data. As such, this finding has the potential to change the way in  
462 which surface chemistry is viewed in the design of new materials based on plant-related natural  
463 surfaces. This is the first time such an analysis has shown the importance of surface chemistry  
464 in a range of leaf types and our produced model can be utilised to investigate and predict the  
465 water contact angle of a range of biological surfaces.

466

## 467 **CONCLUSIONS**

468         The physicochemical, chemical, and topographical properties of leaves obtained from  
469 twelve diverse plant varieties were examined and the results demonstrated that the most  
470 hydrophobic surfaces had low carbonyl species, ordered platelet-like structures, high roughness  
471 values, high  $\gamma_s$  and  $\gamma_s^{LW}$  values, and low  $\gamma_s^{AB}$  and  $\gamma_s^-$  values. However, regardless of the surface

472 properties, all the leaves were self-cleaning. Using PCA, when categorising the samples  
473 according to their chemical classification, it was observed that the more hydrophobic leaves  
474 shared common surface chemistry traits, demonstrated by being grouped in close proximity  
475 with low intra-class variability. In contrast, the less hydrophobic leaves had highly-variable  
476 surface chemistry as measured by ATR-FTIR. Nevertheless, this variability in surface  
477 chemistry was able to accurately model, through PLSR, leaf water contact angle with excellent  
478 ability. This is first time that the importance of surface chemistry in a range of leaf types has  
479 been demonstrated. As such, these results may change the way that surface chemistry is viewed  
480 in the design of new biomimetic materials based on plant surfaces. Furthermore, the presented  
481 model could be used for the fast screening and determination of the water contact angles of a  
482 range of biological surfaces.

483         Extensive work has been carried out on fabricating surfaces with well-defined  
484 topographical features to produce hydrophobic and self-cleaning properties. However,  
485 examples taken from nature clearly demonstrate that less hydrophobic, almost featureless  
486 surfaces may also possess self-cleaning and non-wetting properties. A complete understanding  
487 of the interactions between the magnitude and shape of surface topography, chemistry, and  
488 physiochemistry, in addition to their influence on the self-cleaning action of surfaces has still  
489 not been elucidated. In future work, we intend to design novel surfaces based on these  
490 parameters and assess their self-cleaning properties in a range of experimental assays to  
491 determine their use in specific, applied applications.

492

## 493 **FUNDING**

494         This research did not receive any specific grant from funding agencies in the public,  
495 commercial, or not-for-profit sectors.

496

497 **ASSOCIATED CONTENT**

498 The Supporting Information is available free of charge at

499 Table providing surface free energy components of test liquids; Graphs predicting the  
500 WCAs from the ATR-FTIR using PLSR.

501

502 **CONFLICTS OF INTEREST**

503 The authors declare no competing financial interest.

504

505 **REFERENCES**

- 506 (1) Hsu, S.-H.; Woan, K.; Sigmund, W. Biologically Inspired Hairy Structures for  
507 Superhydrophobicity. *Mater. Sci. Eng. R Reports* **2011**, *72*, 189–201.  
508 <https://doi.org/10.1016/j.mser.2011.05.001>.
- 509 (2) Wang, G.; Guo, Z.; Liu, W. Interfacial Effects of Superhydrophobic Plant Surfaces: A  
510 Review. *J. Bionic Eng.* **2014**, *11*, 325–345. [https://doi.org/10.1016/S1672-](https://doi.org/10.1016/S1672-6529(14)60047-0)  
511 [6529\(14\)60047-0](https://doi.org/10.1016/S1672-6529(14)60047-0).
- 512 (3) Barthlott, W.; Mail, M.; Neinhuis, C. Superhydrophobic Hierarchically Structured  
513 Surfaces in Biology: Evolution, Structural Principles and Biomimetic Applications.  
514 *Philos. Trans. R. Soc. A Math. Phys. Eng. Sci.* **2016**, *374*, 20160191.  
515 <https://doi.org/10.1098/rsta.2016.0191>.
- 516 (4) Barthlott, W.; Neinhuis, C. Purity of the Sacred Lotus, or Escape from Contamination  
517 in Biological Surfaces. *Planta* **1997**, *202*, 1–8. <https://doi.org/10.1007/s004250050096>.
- 518 (5) Peter, A.; Lutey, A. H. A.; Faas, S.; Romoli, L.; Onuseit, V.; Graf, T. Direct Laser  
519 Interference Patterning of Stainless Steel by Ultrashort Pulses for Antibacterial

- 520 Surfaces. *Opt. Laser Technol.* **2020**, *123*, 105954.  
521 <https://doi.org/10.1016/j.optlastec.2019.105954>.
- 522 (6) Rajab, F. H.; Liauw, C. M.; Benson, P. S.; Li, L.; Whitehead, K. A. Production of  
523 Hybrid Macro/Micro/Nano Surface Structures on Ti6Al4V Surfaces by Picosecond  
524 Laser Surface Texturing and Their Antifouling Characteristics. *Colloids Surfaces B  
525 Biointerfaces* **2017**, *160*, 688–696. <https://doi.org/10.1016/j.colsurfb.2017.10.008>.
- 526 (7) Rajab, F. H.; Liauw, C. M.; Benson, P. S.; Li, L.; Whitehead, K. A. Picosecond Laser  
527 Treatment Production of Hierarchical Structured Stainless Steel to Reduce Bacterial  
528 Fouling. *Food Bioprod. Process.* **2018**, *109*, 29–40.  
529 <https://doi.org/10.1016/j.fbp.2018.02.009>.
- 530 (8) Lutey, A. H. A.; Gemini, L.; Romoli, L.; Lazzini, G.; Fuso, F.; Faucon, M.; Kling, R.  
531 Towards Laser-Textured Antibacterial Surfaces. *Sci. Rep.* **2018**, *8*, 10112.  
532 <https://doi.org/10.1038/s41598-018-28454-2>.
- 533 (9) Aryal, B.; Neuner, G. Leaf Wettability Decreases along an Extreme Altitudinal  
534 Gradient. *Oecologia* **2010**, *162*, 1–9. <https://doi.org/10.1007/s00442-009-1437-3>.
- 535 (10) Ensikat, H. J.; Ditsche-Kuru, P.; Neinhuis, C.; Barthlott, W. Superhydrophobicity in  
536 Perfection: The Outstanding Properties of the Lotus Leaf. *Beilstein J. Nanotechnol.*  
537 **2011**, *2*, 152–161. <https://doi.org/10.3762/bjnano.2.19>.
- 538 (11) Balsdon, J. A.; Braman, S. K.; Espelie, K. E. Biology and Ecology of Anagrus  
539 Takeyanus (Hymenoptera: Mymaridae), an Egg Parasitoid of the Azalea Lace Bug  
540 (Heteroptera: Tingidae). *Environ. Entomol.* **1996**, *25*, 383–389.  
541 <https://doi.org/10.1093/ee/25.2.383>.
- 542 (12) Wang, Y.; Braman, S. K.; Robacker, C. D.; Latimer, J. G.; Espelie, K. E. Composition

- 543 and Variability of Epicuticular Lipids of Azaleas and Their Relationship to Azalea  
544 Lace Bug Resistance. *J. Am. Soc. Hortic. Sci.* **1999**, *124*, 239–244.  
545 <https://doi.org/10.21273/jashs.124.3.239>.
- 546 (13) Jetter, R.; Schäffer, S.; Riederer, M. Leaf Cuticular Waxes Are Arranged in  
547 Chemically and Mechanically Distinct Layers: Evidence from *Prunus Laurocerasus* L.  
548 *Plant, Cell Environ.* **2000**, *23*, 619–628. [https://doi.org/10.1046/j.1365-](https://doi.org/10.1046/j.1365-3040.2000.00581.x)  
549 [3040.2000.00581.x](https://doi.org/10.1046/j.1365-3040.2000.00581.x).
- 550 (14) Ribeiro da Luz, B. Attenuated Total Reflectance Spectroscopy of Plant Leaves: A Tool  
551 for Ecological and Botanical Studies. *New Phytol.* **2006**, *172*, 305–318.  
552 <https://doi.org/10.1111/j.1469-8137.2006.01823.x>.
- 553 (15) J. A. Hardin; C. L. Jones; P. R. Weckler; N. O. Maness; Madden, R. D. Rapid  
554 Quantification of Spinach Leaf Cuticular Wax Using Fourier Transform Infrared  
555 Attenuated Total Reflectance Spectroscopy. *Trans. ASABE* **2013**, *56*, 331–339.  
556 <https://doi.org/10.13031/2013.42579>.
- 557 (16) Tu, C.-W.; Tsai, C.-H.; Wang, C.-F.; Kuo, S.-W.; Chang, F.-C. Fabrication of  
558 Superhydrophobic and Superoleophilic Polystyrene Surfaces by a Facile One-Step  
559 Method. *Macromol. Rapid Commun.* **2007**, *28*, 2262–2266.  
560 <https://doi.org/10.1002/marc.200700447>.
- 561 (17) Wang, H.; Shi, H.; Li, Y.; Wang, Y. The Effects of Leaf Roughness, Surface Free  
562 Energy and Work of Adhesion on Leaf Water Drop Adhesion. *PLoS One* **2014**, *9*,  
563 e107062. <https://doi.org/10.1371/journal.pone.0107062>.
- 564 (18) van Oss, C. J.; Good, R. J.; Chaudhury, M. K. The Role of van Der Waals Forces and  
565 Hydrogen Bonds in “Hydrophobic Interactions” between Biopolymers and Low  
566 Energy Surfaces. *J. Colloid Interface Sci.* **1986**, *111*, 378–390.



- 567 [https://doi.org/10.1016/0021-9797\(86\)90041-X](https://doi.org/10.1016/0021-9797(86)90041-X).
- 568 (19) van Oss, C. J. Hydrophobicity of Biosurfaces - Origin, Quantitative Determination and  
569 Interaction Energies. *Colloids Surfaces B Biointerfaces* **1995**, *5*, 91–110.  
570 [https://doi.org/10.1016/0927-7765\(95\)01217-7](https://doi.org/10.1016/0927-7765(95)01217-7).
- 571 (20) van Oss, C. J.; Giese, R. F. The Hydrophilicity and Hydrophobicity of Clay Minerals.  
572 *Clays Clay Miner.* **1995**, *43*, 474–477. <https://doi.org/10.1346/CCMN.1995.0430411>.
- 573 (21) Bos, R.; Busscher, H. J. Role of Acid-Base Interactions on the Adhesion of Oral  
574 Streptococci and Actinomyces to Hexadecane and Chloroform - Influence of Divalent  
575 Cations and Comparison between Free Energies of Partitioning and Free Energies  
576 Obtained by Extended DLVO Analysis. *Colloids Surfaces B Biointerfaces* **1999**, *14*,  
577 169–177. [https://doi.org/10.1016/S0927-7765\(99\)00034-X](https://doi.org/10.1016/S0927-7765(99)00034-X).
- 578 (22) Skovager, A.; Whitehead, K.; Wickens, D.; Verran, J.; Ingmer, H.; Arneborg, N. A  
579 Comparative Study of Fine Polished Stainless Steel, TiN and TiN/Ag Surfaces:  
580 Adhesion and Attachment Strength of *Listeria Monocytogenes* as Well as Anti-  
581 Listerial Effect. *Colloids Surfaces B Biointerfaces* **2013**, *109*, 190–196.  
582 <https://doi.org/10.1016/j.colsurfb.2013.03.044>.
- 583 (23) Whitehead, K. A.; Smith, L. A.; Verran, J. The Detection and Influence of Food Soils  
584 on Microorganisms on Stainless Steel Using Scanning Electron Microscopy and  
585 Epifluorescence Microscopy. *Int. J. Food Microbiol.* **2010**, *141*, S125–S133.  
586 <https://doi.org/10.1016/j.ijfoodmicro.2010.01.012>.
- 587 (24) Mirabella, F. M. *Principles, Theory, and Practice of Internal Reflection Spectroscopy*;  
588 2006. <https://doi.org/10.1201/9781003066941-2>.
- 589 (25) Team, R. C. *The R Project For Statistical Computing*. 2015.

- 590 (26) Team, R. C. A Language And Environment For Statistical Computing. 2015.
- 591 (27) Wickham, H. Elegant Graphics For Data Analysis. 2016.
- 592 (28) Mevik, B.-H.; Wehrens, R.; Liland, K. H. Suggests, Package ‘Pls.’ 2019.
- 593 (29) Camacho, J.; Picó, J.; Ferrer, A. Data Understanding with PCA: Structural and  
594 Variance Information Plots. *Chemom. Intell. Lab. Syst.* **2010**, *100*, 48–56.  
595 <https://doi.org/10.1016/j.chemolab.2009.10.005>.
- 596 (30) Schulte, A. J.; Droste, D. M.; Koch, K.; Barthlott, W. Hierarchically Structured  
597 Superhydrophobic Flowers with Low Hysteresis of the Wild Pansy (*Viola Tricolor*) -  
598 New Design Principles for Biomimetic Materials. *Beilstein J. Nanotechnol.* **2011**, *2*,  
599 228–236. <https://doi.org/10.3762/bjnano.2.27>.
- 600 (31) Nosonovsky, M.; Bhushan, B. Biomimetic Superhydrophobic Surfaces: Multiscale  
601 Approach. *Nano Lett.* **2007**, *7*, 2633–2637. <https://doi.org/10.1021/nl071023f>.
- 602 (32) Bhushan, B.; Jung, Y. C. Micro- and Nanoscale Characterization of Hydrophobic and  
603 Hydrophilic Leaf Surfaces. *Nanotechnology* **2006**, *17*, 2758–2772.  
604 <https://doi.org/10.1088/0957-4484/17/11/008>.
- 605 (33) Godeau, G.; Laugier, J.-P.; Orange, F.; Godeau, R.-P.; Guittard, F.; Darmanin, T. A  
606 Travel in the *Echeveria* Genus Wettability’s World. *Appl. Surf. Sci.* **2017**, *411*, 291–  
607 302. <https://doi.org/10.1016/j.apsusc.2017.03.192>.
- 608 (34) BOYCE, R. L.; McCUNE, D. C.; BERLYN, G. P. A Comparison of Foliar Wettability  
609 of Red Spruce and Balsam Fir Growing at High Elevation. *New Phytol.* **1991**, *117*,  
610 543–555. <https://doi.org/10.1111/j.1469-8137.1991.tb00959.x>.
- 611 (35) Barthlott, W.; Mail, M.; Bhushan, B.; Koch, K. Plant Surfaces: Structures and  
612 Functions for Biomimetic Innovations. *Nano-Micro Lett.* **2017**, *9*, 23.

613 <https://doi.org/10.1007/s40820-016-0125-1>.

614 (36) Zhang, K.; Li, Z.; Maxey, M.; Chen, S.; Karniadakis, G. E. Self-Cleaning of  
615 Hydrophobic Rough Surfaces by Coalescence-Induced Wetting Transition. *Langmuir*  
616 **2019**, *35*, 2431–2442. <https://doi.org/10.1021/acs.langmuir.8b03664>.

617